Catalysis Science & Technology

ROYAL SOCIETY OF CHEMISTRY

PAPER

View Article Online
View Journal | View Issue

Check for updates

Cite this: *Catal. Sci. Technol.*, 2026, **16**, 2331

Cryogenic electron tomography reveals the mesoporous structure evolution during γ-Al_2O_3 supported Mo and MoNiP catalyst formation

Jason M. J. J. Heinrichs, [ab] Angelina Evtushkova,[a] Jovana Zečević, [c] Thomas Weber,[ad] Heiner Friedrich [be] and Emiel J. M. Hensen *[a]

Heterogeneous catalysts play a central role in numerous industrially and societally relevant processes. Despite the widespread use, a detailed understanding of the support mesoporosity and its transformation during catalyst preparation remains incomplete. In this study, cryogenic electron tomography (cryo-ET) was utilized to resolve the 3D mesopore structure of γ-Al_2O_3 and to assess structural changes induced by oxidic Mo and MoNiP deposition and sulfidation during the preparation of hydrodesulfurization (HDS) catalysts. The intrinsic γ-Al_2O_3 surface and mesopore structure remained largely stable throughout calcination and sulfidation, although cryo-ET revealed subtle variations inaccessible to bulk characterization techniques. Oxidic Mo deposition introduced slight increases in tortuosity and surface corrugation, whereas oxidic MoNiP deposition induced minimal changes. Compared to the bare support, sulfidation of both Mo and MoNiP supported on γ-Al_2O_3 resulted in more tortuous mesopores and a more corrugated surface. Careful segmentation enabled separate analysis of γ-Al_2O_3 and MoS_2 slabs, revealing that, for both catalysts, the γ-Al_2O_3 exhibited similar surface and mesopore modifications, and there were no significant differences in MoS_2 slab morphology. Corrected Mo loadings derived from cryo-ET aligned with bulk measurements, validating the approach. These findings provide a comprehensive 3D perspective on mesopore stability during catalyst preparation and highlight the need for higher-resolution imaging and advanced 3D analysis to establish robust structure–function correlations.

Received 21st November 2025,
Accepted 25th February 2026

DOI: 10.1039/d5cy01396h

rsc.li/catalysis

Open Access Article. Published on 05 2569. Downloaded on 14/5/2569 21:12:59.
This article is licensed under a Creative Commons Attribution 3.0 Unported Licence.

Introduction

Ceramic high-surface area mesoporous materials are extensively utilized as support materials in heterogeneous catalysts, which makes them one of the most important classes of industrially employed materials. Heterogeneous catalysts consist of active particles, which are dispersed across and supported on a porous high-surface-area support material. The pore structure and topology of the support material significantly affect the distribution, shape, and accessibility of the deposited active constituents. Consequently, these support properties directly affect the performance of the active catalyst, including reactivity, selectivity, or stability.[1]

Prominent examples of industrial supports are high-surface-area variations of alumina, titania, zirconia, and silica, which can be optimized regarding porosity and other key properties, such as swelling or mechanical and thermal stability.[1] The stability of support materials under operating conditions, such as high temperature and pressure, has been a subject of research interest since the 1990s.[2,3] These research outcomes have largely contributed to the development of industrial catalysts with support pore structures and topologies engineered to the needs of the catalytic reaction. However, a detailed understanding of the mesopore-level structure and how it evolves during support manufacturing and catalyst preparation remains incomplete. Filling this gap would enable catalyst manufacturers to further optimize catalyst design and performance.

A typical method to prepare heterogeneous catalysts is incipient wetness impregnation (IWI). Here, a porous support material is impregnated with a solution that contains active constituents, followed by drying. Depending on the type of catalyst, subsequent heat-treatment steps under different gas compositions may follow. During drying, the dissolved

[a] *Laboratory of Inorganic Materials and Catalysis, Department of Chemical Engineering and Chemistry, Eindhoven University of Technology (TU/e), Den Dolech 2, 5600 MB Eindhoven, The Netherlands. E-mail: e.j.m.hensen@tue.nl*
[b] *Center for Multiscale Electron Microscopy, Department of Chemical Engineering and Chemistry, Eindhoven University of Technology (TU/e), Den Dolech 2, 5600 MB Eindhoven, The Netherlands*
[c] *Shell Global Solutions International B.V, Grasweg 31, 1031 HW Amsterdam, The Netherlands*
[d] *Retired from Shell Global Solutions International B.V, Grasweg 31, 1031 HW Amsterdam, The Netherlands*
[e] *Laboratory of Physical Chemistry, Department of Chemical Engineering and Chemistry, Eindhoven University of Technology (TU/e), Den Dolech 2, 5600 MB Eindhoven, The Netherlands*

Open Access Article. Published on 05 2569. Downloaded on 14/5/2569 21:12:59.
This article is licensed under a Creative Commons Attribution 3.0 Unported Licence.

species precipitate on the support surface according to the support's topology and its chemical interactions with the precipitates, potentially altering the intrinsic support network. Subsequent preparation steps, such as calcination or reduction, yield oxides or metals, respectively, and may lead to morphological changes in the deposited materials, which could alter the pore network of the catalyst. Additionally, calcination or reduction could change the intrinsic support pore network too, but this has not been thoroughly studied yet.

The processing steps during support manufacturing, catalyst preparation, and post-treatment steps can alter the three-dimensional (3D) surface and mesopore structure of the support and the catalyst. For example, the temperature used during the preparation of SBA-15 support particles determines the size of the (dis)ordered pores.[4] Additionally, hydrothermal post-treatments can alter the mesopore connectivity and accessibility of ceria–zirconia oxides.[5,6] Ultimately, the surface and pore structure of the support influences the particle morphology and location of the active particle, while the accessibility of the active particle is governed by the total catalyst pore network. Both aspects influence catalytic performance. Therefore, it is important to follow the support and catalyst surface and pore structure during catalyst preparation and post-treatment steps, which is the focus of this study.

We selected Mo(NiP) supported on disordered mesoporous γ-Al_2O_3 due to extensive prior research and the potential for future sustainable applications. Typically prepared through IWI followed by calcination and sulfidation, this catalyst class has been optimized over several decades primarily for hydrodesulfurization (HDS), the key industrial process for removing sulfur from crude oil. Ni-promoted Mo/γ-Al_2O_3 catalysts exhibit significantly higher HDS activity than their non-promoted counterparts, as Ni forms Ni–Mo–S species located at the edges of MoS_2 slabs, thereby enhancing catalytic performance.[7,8] Phosphorus is frequently added as a modifier because it partially passivates the acidic surface sites of γ-Al_2O_3 through the formation of aluminum phosphate species.[9–13] This passivation weakens the strong metal–support interaction between Mo(Ni) species and γ-Al_2O_3. Moreover, P enhances the formation of type II MoS_2 slabs, which possess higher intrinsic activity than type I slabs.[13–15]

A considerable body of research has explored various aspects of (promoted) MoS_2/γ-Al_2O_3. This includes nanoscale visualization through transmission electron microscopy (TEM) and electron tomography (ET),[16–19] characterization of porous architectures through X-ray computed tomography,[20,21] studies on MoS_2 slab morphology,[14,22,23] investigations of pore and support effects on slab structure and catalytic performance,[24–28] analyses of the liquid-impregnation process during catalyst preparation,[29,30] studies of the effect of additives on (promoted) oxidic Mo catalysts,[15,31–36] and the sulfidation process.[33,37–40]

More recently, MoS_2-based catalysts have shown promising applications beyond HDS, including biomass upgrading,[38,41–44] primarily hydrodeoxygenation (HDO),[38,41] CO_2 hydrogenation to methanol,[45] and the water–gas shift reaction in sulfur-containing synthesis gas obtained by biomass gasification.[46,47] γ-Al_2O_3 continues to be one of the most-widely used catalyst supports,[48] raising important questions about the stability of γ-Al_2O_3, especially regarding its susceptibility to support dissolution during aqueous impregnation[1,48] and subsequent preparation steps. Ultimately, a detailed understanding of how the pore structure of the support evolves throughout the catalyst preparation sequence is still lacking.

The pore size and structure of mesoporous materials can be probed using both indirect and direct methodologies. Indirect techniques such as Hg porosimetry and N_2 physisorption enable estimation of the pore size distribution and pore volume by quantifying the amount of Hg intruded or N_2 adsorbed.[49–52] Additionally, N_2 physisorption combined with a quantitative analytical method, such as liquid chromatography or differential scanning calorimetry (DSC), can be used to identify diffusion regimes[53] or pore blocking phenomena[54] at the bulk scale. While bulk characterization techniques provide insights into structural, electronic, and chemical properties of catalyst materials,[29,30,55–61] ET offers direct three-dimensional visualization and quantitative analysis of catalyst morphology and mesopore architecture. For example, Arslan *et al.* (2008) demonstrated using ET that the support strongly influences the final catalyst morphology,[62] and Nan *et al.* (2011) obtained nanospatial information on MoS_2 slabs in a MoS_2/SiO_2 catalyst.[63] However, to date, ET has not been applied to investigate the evolution of mesopore structure in γ-Al_2O_3-supported Mo catalysts during preparation.

Here, we study the pore structure of bare γ-Al_2O_3 during the different stages of IWI preparation, including calcination and sulfidation, as well as the structural changes that occur upon deposition of oxidic Mo or MoNiP precursors, followed by subsequent sulfidation. To this end, we employ cryogenic ET (cryo-ET), which provides 3D, nanometer-scale visualization of surface and pore structures. This approach enables both qualitative and quantitative analysis of pore morphology and, when catalytic phases can be distinguished from the support, the assessment of particle morphology and distribution within the porous network.[5,64–72] Complementary characterization techniques, including N_2 physisorption, synchrotron X-ray diffraction, and X-ray photoelectron spectroscopy, are used to validate and further contextualize the structural insights obtained from ET.

This study aims to develop a comprehensive structural understanding of Mo-based catalysts throughout their preparation. The insights generated are intended to support the rational design of Mo-based catalysts for emerging applications beyond well-established hydrotreating processes, for which the superior performance of MoNiP/γ-Al_2O_3 catalysts is already extensively documented. To this end, Mo/γ-Al_2O_3 and MoNiP/γ-Al_2O_3 are systematically compared to evaluate whether structural differences can be directly

 This journal is © The Royal Society of Chemistry 2026

Open Access Article. Published on 05 2569. Downloaded on 14/5/2569 21:12:59.
This article is licensed under a Creative Commons Attribution 3.0 Unported Licence.

visualized using cryo-ET and to relate these nanoscale observations to established structural models.

Our results reveal that the intrinsic structural and electronic features of bare γ-Al_2O_3 are preserved after calcination and sulfidation, establishing a baseline for comparison of bare and Mo or MoNiP-filled γ-Al_2O_3. Initial observations indicate differences between Mo and MoNiP-filled γ-Al_2O_3 in terms of surface and pore structure descriptors, but notably, sulfidation results in similar surfaces, pores, and active phase descriptors.

Experimental

Catalyst preparation

A γ-Al_2O_3 support (Ketjen, CK300) was used for catalyst preparation. This material contains a disordered network of mesopores and has a H_2O pore volume of 0.62 cm^3 g^{-1}. It is supplied as cylindrical extrudates with a diameter of 1 mm and a length of 3–10 mm. This support is produced commercially using a proprietary process that involves acid-peptization of pseudo-boehmite, extrusion of the resulting paste, followed by controlled drying, and calcination at intermediate temperatures. Catalysts were prepared by incipient wetness impregnation (IWI) on the γ-Al_2O_3 extrudates (Table 1). MoNiP/γ-Al_2O_3 was prepared using a metal salt solution obtained by mixing H_3PO_4 (85%) and MilliQ water (3 mL), followed by the addition and dissolution of MoO_3 and $NiCO_3$. Next, the solution was heated to 100 °C until a transparent green solution was obtained. To prepare Mo/γ-Al_2O_3, a metal salt solution was prepared by dissolving MoO_3 in ammonium hydroxide (32% NH_3 in H_2O). MilliQ water was added to both precursor solutions to reach a total volume of 5 mL. These solutions were then used to impregnate the γ-Al_2O_3 extrudates. The impregnated extrudates were rotated on a roller bank in a sealed vial for ~2 h, after which they were transferred to a ceramic crucible covered with perforated aluminium foil to allow drying in air at ambient temperature. The crucible was then placed in an oven overnight at 120 °C to ensure complete Solvent removal. The crucible was then placed in a calcination oven, where the material was heated to 400 °C for 2 h (ΔT = 6 °C min^{-1}). Single-stage sulfidation was performed according to traditional model conditions to ensure simplicity, reproducibility and consistency with previously reported structural studies on similar catalysts.[20,22,73–75] Sulfidation was performed in a stainless-steel reactor with an inner diameter of 4 mm. In detail, ~75 mg of a crushed sieved fraction (75–125 μm) mixed with 200 mg SiC were loaded in the middle of the reactor and sulfided at ambient pressure for 2 h at 350 °C (ΔT = 6 °C min^{-1}) in a 50 mL min^{-1} flow of 10 vol% H_2S in H_2. After sulfidation, the sample was transferred to a glovebox without air exposure until further characterization.

(cryo-)TEM and ET sample preparation

TEM grids of 200 mesh Cu with a 6 nm thick continuous carbon layer were used for all measurements. Sample preparation involved gently crushing the catalyst extrudates into a fine powder, which was then dispersed in absolute ethanol. A small aliquot of the suspension was drop-cast onto a Au back-labelled TEM grid and allowed to dry, enabling the particles to adhere to the carbon layer. As a result, the particles remain attached to the carbon layer and thus ensuring stable imaging conditions.[76] Preparation of sulfided TEM samples was performed entirely inside the glovebox to prevent exposure to air.

(cryo-)TEM, ET, and STEM-EDX data acquisition

TEM images and tilt series were acquired on a Glacios cryo-TEM (TFS, Thermo Fisher Scientific) operated at 200 kV, equipped with a direct electron detector (FALCON 4i). For best results in (cryo-)TEM and (cryo-)ET, particles were selected with a thickness and width in the 100–300 nm range. 4 K tilt series, were acquired at a magnification of 92 k× (pixel size = 0.1535 nm) or 150 k× (pixel size = 0.0942 nm) within an angular range of −68° to 68° at increments of 1° and a nominal defocus of −1.0 μm (at 92 k×) or −0.2 μm (at 150 k×). At 92 k×, the dose rate was ~5.1 e^- $Å^{-2}$ image and the exposure time 0.3 s. At 150 k×, the dose rate was ~9.0 e^- $Å^{-2}$ · image and the exposure time 1.18 s. Potential beam damage was evaluated by acquiring images before and after the tilt series. No detrimental beam effects were observed at the used total dose.

STEM-EDX mapping was performed on a Titan Themis (FEI/TFS) operated at 300 kV and equipped with an XFlash 6 T|60 (Bruker) EDS detector. Elemental EDX maps were acquired at 40 k× with a beam convergence angle of 9.5 mrad and a camera length of 160 mm. Frames of approximately 450 × 450 pixels with a dwell time of 32 μs were recorded for 20 minutes. STEM-EDX maps were averaged by a [3 3] kernel prior to further analysis. K-edge quantification was performed with the Cliff-Lorimer method on Al, O, Mo, Ni, P, and S.

3D reconstruction and 3D quantitative analysis

Tilt-series alignment and tomographic reconstructions were performed in IMOD.[77–79] In general, the aligned stacks (137

Table 1 Details regarding the IWI preparation of γ-Al_2O_3 supported Mo and MoNiP catalysts

Catalyst	MoO_3 (g)	$NiCO_3$ (g)	H_3PO_4 (g)	γ-Al_2O_3 (g)	Intended loading (wt%) Mo	Ni	P
Mo/γ-Al_2O_3	1.42	—	—	8.06	10	—	—
MoNiP/γ-Al_2O_3	1.53	0.50	0.51	8.06	10	2.4	1.3

Open Access Article. Published on 05 2569. Downloaded on 14/5/2569 21:12:59.
This article is licensed under a Creative Commons Attribution 3.0 Unported Licence.

images with 1° tilt increments) were binned by a factor of 2. After binning, the final pixel size for the tilt series was 0.19 nm and 0.31 nm at 150 k× and 92 k×, respectively. To reconstruct the 3D volume, the simultaneous iterative reconstruction technique (SIRT) was used for 10 iterations only to prevent the fitting of noisy data, which is a consequence of the low dose used during acquisition. To reduce computational time during quantitative analysis, reconstructed volumes were trimmed to dimensions matching the imaged particle beforehand. The final volume was denoised by applying a 3D median filter with a kernel size of [3 3 3]. This filter preserves edge features present in the original 3D reconstruction.

Next, pixel classification (*i.e.*, segmentation) was performed through ILASTIK.[80,81] Depending on the sample imaged, regions that could be identified as either background (*i.e.*, vacuum), γ-Al_2O_3, Mo/γ-Al_2O_3, MoNiP/γ-Al_2O_3, or MoS_2 were manually annotated. The annotated regions were used to train a random forest classifier. This classifier groups pixels based on 3D-smoothed pixel intensity, edge filters, and texture descriptors. Each reconstruction was segmented by a unique random forest classifier model based on several input images originating from the same reconstruction.

After segmentation, a MATLAB script was used to clean the segmentation (*i.e.*, remove isolated voxels by majority operation, 3 iterations), after which the specific surface area (SSA) was calculated. The average strut width of the solid framework was obtained from the volumetric strut width distribution by multiplying the strut network skeleton by its distance map, both obtained through AMIRA3D. Next, morphological operations were performed to obtain the pore network and pore volume (PV). The pore network skeleton and distance map were obtained through AMIRA3D (TFS). The pore tortuosity (*i.e.*, the path between two pore nodes relative to the straight path) was determined *via* skeletonization in AMIRA3D. The average pore size was obtained from the volumetric pore size distribution (PSD) by multiplying the pore network skeleton by its distance map, also obtained through AMIRA3D. The shape index[82] (*i.e.*, the local surface type: a cup-like (−1), a saddle-like (0), or a dome-like (1) surface) and curvedness[82] (*i.e.*, bending degree of local surface type) of the isosurfaces of the solids were determined in AMIRA3D. Here, the variance of the shape index and curvature defines the corrugation of a surface. The higher the variance, the higher the corrugation, meaning more surface shape type and/or curvature strength fluctuations across a particle. Details regarding the estimation of the total corrugation per individual reconstructed particle are provided in the supplementary section S1. MoS_2 slab descriptors, such as loading, thickness, nearest neighbor distance, perimeter, and interface, were quantified in MATLAB. The weight loading was calculated based on the total voxel volume of each component directly after segmentation. The thickness, nearest neighbor distance, perimeter, and interface were calculated after performing the majority operation. Finally, AMIRA3D was used to render 3D volumes of the reconstructions.

Bulk characterization

N_2 physisorption was used to determine the specific surface area (SSA), pore volume (PV), and pore size distribution (PSD) of the support or catalyst (50–200 mg; powder fraction 75–125 μm). Physisorption measurements were performed at −196 °C in a Micromeritics ASAP 2020 apparatus. Before measurements, all samples, except the sulfided samples, were pretreated in vacuum for 6 h at 100 °C. The pore size distribution (PSD) was determined using the Barrett–Joyner–Halenda (BJH) method, which was applied to the adsorption and desorption isotherms. To enhance accuracy, a Halsey thickness curve was employed, along with the Faas BJH correction, to account for potential deviations and improve the reliability of the pore size analysis. In this study, the PSD is the normalized volumetric contribution of a certain pore range to the total pore volume (dV/dW). It should not be mistaken for the derivative. The SSA was estimated by the Brunauer–Emmet–Teller (BET) method, and the PV was determined from the cumulative pore volume up to 15 nm in diameter, as derived from the BJH adsorption curve.

Inductively coupled plasma optical emission spectroscopy (ICP-OES) was used to analyze the elemental composition of the calcined catalysts. Measurements were carried out using a Spectro CIROS CCD Spectrometer. Typically, approximately 35 mg of the sample was dissolved in a mixture of 2 mL HNO_3 (65%) and 4 mL of a 1 : 1 mixture of H_2SO_4 (97%) and H_2O (1 : 1), with stirring to ensure complete dissolution.

Synchrotron X-ray diffraction (XRD) was used to evaluate the stability of γ-Al_2O_3 by determining its primary particle size after calcination and subsequent sulfidation. Measurements were carried out at the ID22 beamline at the ESRF synchrotron facility in Grenoble, France. Data were collected in transmission mode using an incident X-ray energy of 35 keV (λ = 0.354 Å). The scattered signal was detected with an Eigen2 XCdTe 2 M-W detector, preceded by 13 Si (111) crystals for optimal resolution. Samples were loaded into quartz capillaries (2 mm outer diameter, wall thickness 0.1 mm) and sealed by Beeswax to prevent contamination. Sulfided samples were prepared in a glovebox. The Scherrer equation was used to calculate the crystallite size (*i.e.*, primary particle size) of γ-Al_2O_3.

X-ray photoelectron spectroscopy (XPS) was used to analyze the surface composition, oxidation states, and sulfidation degree. To this end, a K-alpha XPS apparatus (Thermo Scientific) equipped with an aluminum anode (Al Kα = 1486.68) monochromatized X-ray source was used. All samples were finely ground and attached to double-sided carbon tape. Sulfided samples were prepared in a glovebox and transferred into the XPS apparatus *via* an airtight transport vessel. All spectra were recorded using a flood gun to reduce surface charging. By means of the software CasaXPS, a standard procedure involving calibration towards

 This journal is © The Royal Society of Chemistry 2026

Open Access Article. Published on 05 2569. Downloaded on 14/5/2569 21:12:59.
This article is licensed under a Creative Commons Attribution 3.0 Unported Licence.

the Al 2p signal (74.1 eV) and Shirley background subtraction was performed on all spectral data. Fitting was performed with a symmetric pseudo-Voigt function (GL(30)).

Raman spectroscopy was employed to assess the structure, crystallinity, and coordination environment of the metal oxide precursor. Spectra were recorded using a Witec alpha 300 R confocal Raman microscope equipped with a 532 nm diode excitation source, a 1200 lines per mm grating (BLZ = 500 nm), and a charge-coupled device (CCD) was used. A ZEISS LD EC Epiplan-Neofluar Dic 50×/0.55 objective was used. Spectra of the powder samples were collected using 1200 accumulations with an integration time of 1 s per accumulation.

Ultraviolet-visible diffuse reflectance spectroscopy (UV-vis DRS) was used to investigate the coordination and aggregation states of the supported metal oxide phases. Spectra were collected from calcined powder samples (<75 μm) using a Thermo Scientific Evolution Pro UV-vis spectrophotometer. A spectral bandwidth of 1.5 nm, a measurement interval of 0.5 nm, and an integration time of 0.5 s were applied. $BaSO_4$ served as the reflectance standard. The electronic edge energy (E_g) of ligand-to-metal charge transfer transitions was determined from the intercept of the energy-axis and the tangent line of $[F(R_\infty)h\nu]^2$ *vs.* $h\nu$ plot, where $F(R_\infty)$ is the Kubelka–Munk function and $h\nu$ is the photon energy.

Temperature-programmed reduction (TPR) was performed to study the reducibility of the samples. Experiments were performed on a Micromeritics AutoChem II instrument by loading 100 mg of powder (75–125 μm fraction) into a quartz U-tube reactor, positioned between two layers of quartz wool. Prior to analysis, the samples were pretreated at 200 °C for 1 h in a flow of 50 mL min^{-1} He. TPR profiles were recorded by heating the sample from 40 °C to 900 °C at a 5 °C min^{-1} rate in a 50 mL min^{-1} flow of 4 vol% H_2 in N_2. H_2 consumption was monitored by a thermal conductivity detector (TCD), which was calibrated with an AgO reference.

Results and discussion

Bare γ-Al_2O_3 supports (untreated, calcined, and sulfided)

To determine whether the pore structure of the γ-Al_2O_3 support changes during catalyst preparation, it is essential to investigate the bare support prior to and after each synthesis step, namely the untreated, calcined, and sulfided states. Over years of storage and handling, untreated γ-Al_2O_3 is exposed to air and humidity, resulting in re-hydroxylation of the surface and equilibration with ambient conditions. To refresh the support surface and thereby remove physisorbed water, regenerate hydroxyl groups, and eliminate contaminants, the untreated γ-Al_2O_3 was calcined prior to use. Accordingly, we deemed it necessary to evaluate the stability of the γ-Al_2O_3 mesopore structure at the nanoscale after both the calcination and sulfidation steps. Ideally, many datasets would be averaged to yield a statistically robust distribution of quantitative pore structure descriptors. However, such extensive data collection is currently impractical with cryo-ET due to substantial time required for acquisition, processing, and analysis. To balance experimental feasibility with statistical relevance, each sample state was therefore imaged in triplicate.

Previous work has shown that the untreated bare γ-Al_2O_3 used in this study exhibits regions with different pore structures.[83] Fig. 1(a–c) displays numerical cross sections through the reconstructions of untreated, calcined, and sulfided γ-Al_2O_3 support particles. Additionally, numerical cross sections from the top, middle, and bottom regions of all reconstructed particles are shown in SI section S2. Among the states, the observed particles varied in size, which can be attributed to the crushing of the extrudates during TEM sample preparation. Variations in the packing density and size of the fused γ-Al_2O_3 primary particles were observed, which are expected to lead to differences in pore structure descriptors. These variations are not attributed to calcination or sulfidation, as they were observed in the pristine material too (Fig. S2.1). No other visual differences were observed between the states, while quantifying the cryo-ET data can provide a much more detailed description of the mesopore network and possible effects of calcination and sulfidation.

To obtain quantitative insights into the γ-Al_2O_3 pore structure, the support structure was isolated (segmented) from the reconstructed cryo-ET data, resulting in a binary 3D dataset for detailed analysis (Fig. S2.4). For each state, surface and pore structure descriptors of three unique segmented 3D datasets, representing individual γ-Al_2O_3 support particles, were quantified and averaged to assess the preservation of the support. Additionally, bulk characterization techniques were employed to determine the preservation of the main physicochemical properties of the γ-Al_2O_3 throughout the preparation process.

The bulk pore structure was estimated by N_2 physisorption. As shown in Fig. S3.1(a), the untreated, calcined, and sulfided γ-Al_2O_3 samples exhibit a type IV(a) isotherm, characteristic of mesoporous materials.[50] The adsorption–desorption branches and the associated hysteresis loops indicate that the overall pore structures of the three γ-Al_2O_3 states appear very similar. In contrast, the averaged cryo-ET data, shown in Fig. 1(d and e), reveal pronounced differences in pore volume (PV), pore size (distribution in Fig. S2.5), specific surface area (SSA), and strut width among the states. These variations corroborate the qualitative differences evident from visual inspection of the reconstructions.

For each state, the PV derived from cryo-ET (Fig. 1(d)) is significantly smaller than the PV derived from N_2 physisorption analysis (Fig. S3.1(b)). This discrepancy likely arises from fracturing of the structure along the largest pores during sample preparation, where grinding may preferentially open wide pores. As a result, these larger pores are no longer enclosed volumes and are therefore not captured in the PV determination by cryo-ET. The PV measured by cryo-ET remains essentially constant following

Open Access Article. Published on 05 2569. Downloaded on 14/5/2569 21:12:59.
This article is licensed under a Creative Commons Attribution 3.0 Unported Licence.

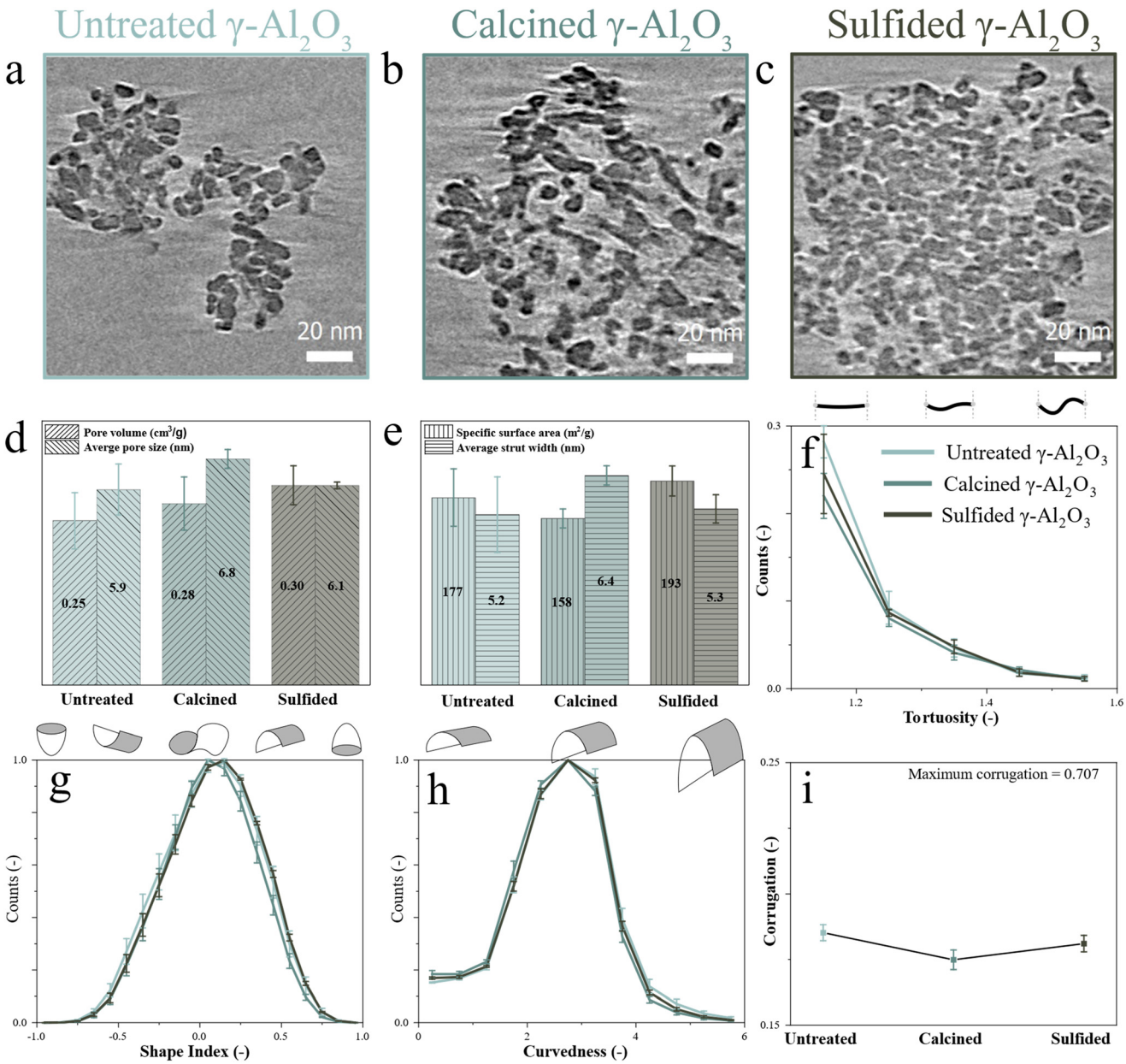

Fig. 1 Quantitative ET showing numerical cross sections (thickness = 0.31 nm) through cryo-ET reconstructions of bare γ-Al_2O_3 supports in (a) untreated, (b) calcined, and (c) sulfided state (each triplo). Quantitative analysis of the surface and pore network showing the averaged values for: (d) PV and average pore size; (e) SSA and average strut width; (f) tortuosity; (g) shape index, (h) curvedness, and (i) corrugation.

calcination and sulfidation. For each state, the average pore size estimated by cryo-ET (Fig. 1(d)) is in good agreement with the desorption BJH pore size distributions (Fig. S3.1(d)). Additionally, the SSA calculated from cryo-ET (Fig. 1(e)) matches well the BET results (Fig. S3.1(b)). Finally, for each state, the average strut width, measured by cryo-ET (Fig. 1(e)), showed variations from 4.0 to 6.7 nm. This aligns with the presence of a range of primary γ-Al_2O_3 platelet sizes at every state. The application of the Scherrer equation to the synchrotron XRD data revealed crystallite sizes ranging from 4.2 to 8.4 nm for the untreated and calcined γ-Al_2O_3 and 4.0 to 8.4 nm for the sulfided γ-Al_2O_3 (Fig. S3.3 and Table S3.2). These results suggest that the primary γ-Al_2O_3 platelets remain stable during calcination and sulfidation.

In addition, cryo-ET enabled a more detailed analysis of structural features that were not directly accessible by bulk characterization. In Fig. 1(f–i), the tortuosity, shape index, curvedness, and corrugation of untreated, calcined, and sulfided γ-Al_2O_3 are shown. These descriptors exhibit only minor variations with overlapping error ranges. Therefore, the structural features of bare γ-Al_2O_3 appear to be preserved following calcination and sulfidation.

Based on the combined assessment of the cryo-ET data and bulk characterization results, γ-Al_2O_3 appears structurally stable after both calcination and sulfidation.

 This journal is © The Royal Society of Chemistry 2026

Open Access Article. Published on 05 2569. Downloaded on 14/5/2569 21:12:59.
This article is licensed under a Creative Commons Attribution 3.0 Unported Licence.

The observed variations in surface and pore descriptors are therefore more attributed to intrinsic local heterogeneity of the support, heterogeneity that cryo-ET is uniquely sensitive to, rather than from systematic modification of the γ-Al_2O_3 framework. Moreover, the combined set of descriptors obtained for each particle can be used to construct a structural model of the pore architecture, which can be used to illustrate the relation among individual descriptors (SI section S4). To establish a reference for the intrinsic structural heterogeneity of the bare γ-Al_2O_3, the average values from the untreated, calcined, and sulfided datasets, comprising a total of 9 reconstructed particles, are used as a baseline for comparison with Mo or MoNiP-containing γ-Al_2O_3 samples, which will be discussed in the next section.

γ-Al_2O_3 supported Mo or MoNiP after calcination and sulfidation

This section examines the changes in surface and pore structure following the deposition of oxidic Mo or MoNiP on γ-Al_2O_3 supports and subsequent sulfidation. To ensure a fair comparison, the intended Mo weight loading for both Mo/γ-Al_2O_3 and MoNiP/γ-Al_2O_3 is 10 wt%. The actual Mo loadings of the calcined samples were characterized using ICP-OES, XPS, and STEM-EDX, with results shown

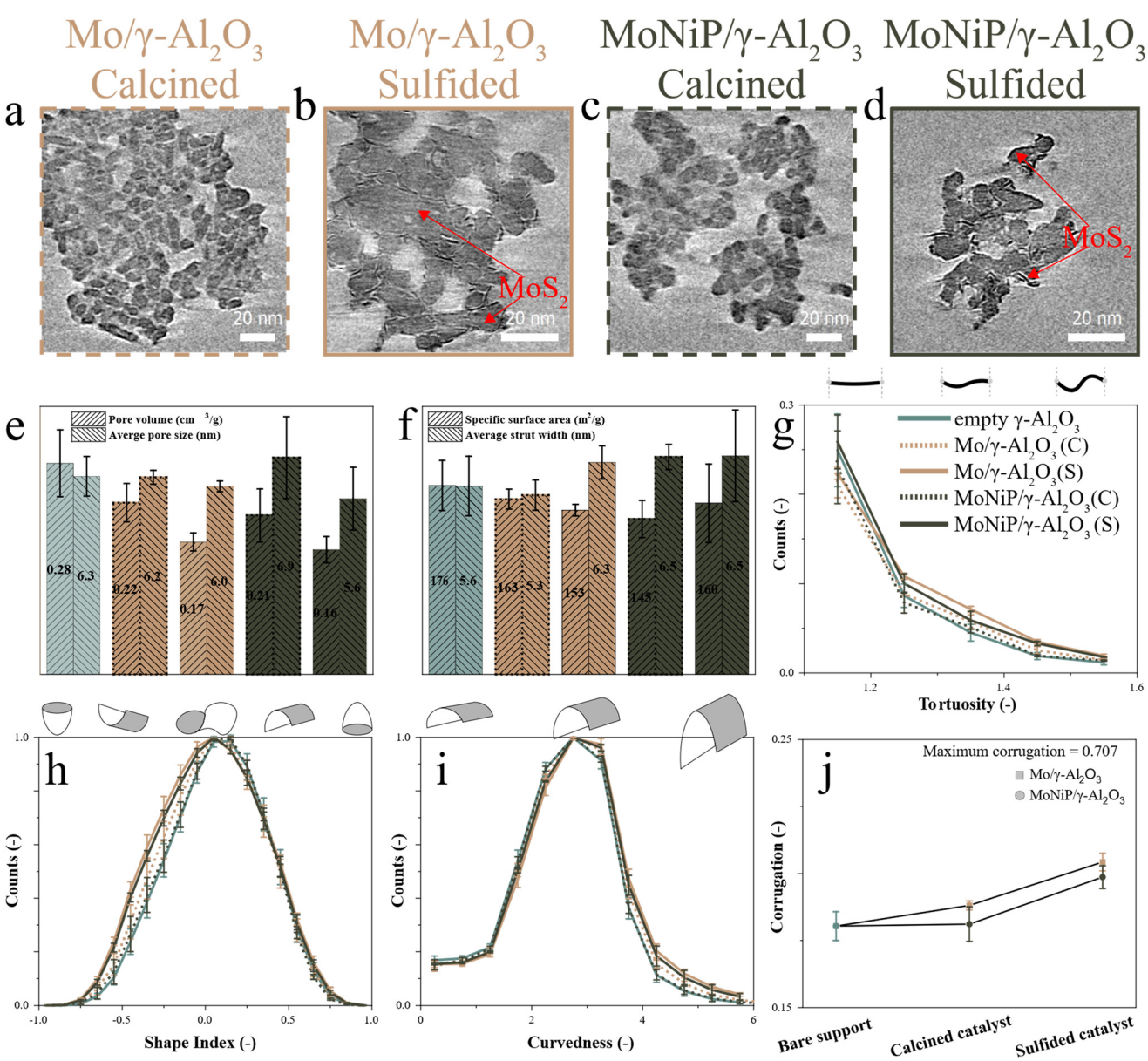

Fig. 2 Quantitative ET showing numerical cross sections ((a and c) thickness = 0.31 nm; (b and d) thickness = 0.19 nm) through cryo-ET reconstruction of calcined (a and c) and sulfided (b and d) Mo/γ-Al_2O_3 and MoNiP/γ-Al_2O_3. An enlarged image of (a–d) is shown in Fig. S5.1(a–d). The formed MoS_2 particles are indicated by red arrows. Quantitative analysis of the surface and pore network showing: (e) PV and average pore size; (f) SSA and average strut width; (g) tortuosity; (h) shape index, (i) curvedness; and (j) surface corrugation.

Open Access Article. Published on 05 2569. Downloaded on 14/5/2569 21:12:59.
This article is licensed under a Creative Commons Attribution 3.0 Unported Licence.

in the SI (Tables S3.5 and S3.6). Moreover, as shown in Fig. S3.7(a) and S3.8(a), STEM-EDX reveals a uniform sub-micron-level distribution of the calcined Mo in Mo/γ-Al_2O_3 and of calcined Mo, Ni, P in MoNiP/γ-Al_2O_3.

Numerical cross sections of calcined and sulfided Mo/γ-Al_2O_3 are shown in Fig. 2(a and b), with an enlarged view in Fig. S5.1(a and b). Cross sections from the top, middle, and bottom regions of all reconstructed Mo/γ-Al_2O_3 particles are shown in Fig. S5.2 and S5.3. The calcined Mo/γ-Al_2O_3 particles exhibit a similar structure to the bare γ-Al_2O_3, where the fused primary particles form the porous backbone. The absence of features that could be associated with segregated Mo oxide particles indicates that oxidic Mo is uniformly dispersed at the nanometer scale across the γ-Al_2O_3 surface. Due to this uniform distribution, insufficient contrast existed between the two materials for the oxidic Mo to be identified. After sulfidation, the structure of the primary γ-Al_2O_3 particles changed, and oxidic Mo transformed into MoS_2 slabs visible on the surface of the γ-Al_2O_3 (Fig. 2(a and c)). A variety of basal and edge plane connections between the slabs and γ-Al_2O_3, combined with minimal slab stacking, were observed. Similar observations were made for the numerical cross sections of calcined and sulfided MoNiP/γ-Al_2O_3, shown in Fig. 2(c and d), with an enlarged view in Fig. S5.1(c and d) and cross sections from the top, middle, and bottom regions of all reconstructed MoNiP/γ-Al_2O_3 particles in Fig. S5.4 and S5.5. How and to what extent the deposition of calcined Mo or MoNiP and subsequent sulfidation change the pore structure with respect to the bare γ-Al_2O_3 will be discussed in the next section.

To extract surface and mesopore structure descriptors inaccessible through visual interpretation alone, the solid material depicted in Fig. 2(a–d) was segmented. Slices of the segmented volumes are shown in Fig. S5.6. Descriptors were extracted for three distinct Mo/γ-Al_2O_3 and MoNiP/γ-Al_2O_3 particles, with results averaged for the calcined and sulfided states, and compared to initially bare γ-Al_2O_3. Bulk characterization techniques were employed to assess the primary physicochemical properties following solids deposition and sulfidation.

The effect of deposition of both oxidic Mo and MoNiP (*i.e.*, the calcined state) on the γ-Al_2O_3 surface, as well as the following sulfidation, resulted in different surface and mesopore structures compared to the initially bare γ-Al_2O_3. As shown in Fig. 2(e), a similar decrease in PV occurred after the deposition of oxidic Mo or MoNiP and sulfidation. Additionally, the bulk PV decreased similarly after solids deposition (Fig. S3.1 and Table S3.1), suggesting preferential deposition of solids in pores ranging from 2 to 15 nm, which are more prevalent in cryo-ET specimens than in the bulk powder. Notably, cryo-ET suggests that after Mo or MoNiP deposition and sulfidation, the average pore size remained within the initial range determined for bare γ-Al_2O_3. This is also observed in the bulk, as BJH analysis of the adsorption and desorption branches, shown in Fig. S3.1(c and d), does not reveal a significant decrease in the PSD after solids deposition or sulfidation.

In Fig. 2(f), the SSA and average strut width after solids deposition and subsequent sulfidation are depicted. The subtle trends in SSA resemble those observed in bulk (Fig. S3.1 and Table S3.1), suggesting that the SSA is primarily determined by the mesopores. Moreover, both cryo-ET and bulk show a sequential SSA decrease after solids deposition and sulfidation for Mo/γ-Al_2O_3. In contrast, for MoNiP/γ-Al_2O_3, the SSA decreases after solids deposition but shows a slight increase after sulfidation. In this study, it is not possible to unambiguously assign the observed increase in SSA for Mo/γ-Al_2O_3 and the decrease for MoNiP/γ-Al_2O_3 to specific molecular-level mechanisms. Nevertheless, these trends are likely linked to the broader structural and compositional changes occurring during sulfidation. Formation of MoS_2 involves replacement of O by S, which occupies a larger atomic volume than O in the oxidic Mo species, and visual inspection reveals accompanying changes to the γ-Al_2O_3 framework, altering its pore and surface structure. The presence of Ni and P is expected to influence MoS_2 morphology and may also affect the γ-Al_2O_3 surface after sulfidation compared with Mo-only catalysts. The average strut width, found through cryo-ET, remains within the range observed for the bare γ-Al_2O_3, implying that deposition of Mo or MoNiP does not substantially change the average strut width.

Cryo-ET descriptors inaccessible by bulk characterization revealed distinct differences in the surface and mesopore structure after calcination and sulfidation of the bare γ-Al_2O_3, Mo/γ-Al_2O_3, and MoNiP/γ-Al_2O_3. During calcination, aggregated molybdate structures are expected to form on the γ-Al_2O_3 surface.[84] Fig. 2(g–j) show that, compared to the bare γ-Al_2O_3, the Mo/γ-Al_2O_3 exhibits a more tortuous pore system (*i.e.*, higher tortuosity) and a more corrugated surface (*i.e.*, broadened shape index and curvedness distribution), suggesting the formation of topographically prominent Mo domains. In contrast, the tortuosity and corrugation of MoNiP/γ-Al_2O_3 are similar to the bare γ-Al_2O_3, suggesting that the oxidic MoNiP is distributed as a thin layer that does not alter the pores and surface. This interpretation is consistent with UV-vis DRS, suggesting smaller and thinner Mo aggregates in MoNiP/γ-Al_2O_3 (Fig. S3.5), and Raman displaying more tetrahedrally coordinated (isolated) Mo species in Mo/γ-Al_2O_3 (Fig. S3.6).

H_2-TPR data (Fig. S3.7) reveals that Mo/γ-Al_2O_3 undergoes reduction at higher temperatures and exhibits a pronounced high-temperature bulk-reduction feature, consistent with strong stabilization of Mo–O–Al species. In contrast, MoNiP/γ-Al_2O_3 shows a significant shift of the main reduction peak to lower temperatures and the disappearance of the bulk-reduction signal. This behavior reflects a markedly weakened effective metal–support interaction, arising from suppression of strong Mo–O–Al bonding and the formation of thin Mo–O–P networks near Ni. The presence of Ni and P enhances hydrogen accessibility to Mo species and thus facilitates reduction.

 This journal is © The Royal Society of Chemistry 2026

Open Access Article. Published on 05 2569. Downloaded on 14/5/2569 21:12:59.
This article is licensed under a Creative Commons Attribution 3.0 Unported Licence.

In future work, it will be important to gain insights into the exact location of deposited oxidic species. This requires deposits to be distinguished from the support, which was not possible for the combination of Mo and γ-Al_2O_3 in this study. There are various routes to accomplish this, such as four-dimensional (4D) scanning TEM, integrated differential phase contrast (iDPC) - STEM, or segmentation through deep learning.[70,85,86]

During the sulfidation step, oxidic Mo converts to MoS_2, which is the active catalyst phase. Interestingly, after sulfidation, the pore morphologies of Mo/γ-Al_2O_3 and MoNiP/γ-Al_2O_3 are quite similar yet different from the bare γ-Al_2O_3 (Fig. 2(g–j)). During sulfidation, immobilized MoO_x species are transformed into mobile MoS_x domains, which aggregate and grow into MoS_2 slabs.[84] The resulting MoS_2 particles affect the pore structure of both MoNiP/γ-Al_2O_3 and Mo/γ-Al_2O_3 similarly, suggesting that the MoS_2 particles occupy comparable positions on the γ-Al_2O_3 surface.

Direct quantification of isolated γ-Al_2O_3 and MoS_2 slabs after sulfidation

The previous section showed that the deposition of oxidic Mo or MoNiP, followed by sulfidation, resulted in a different

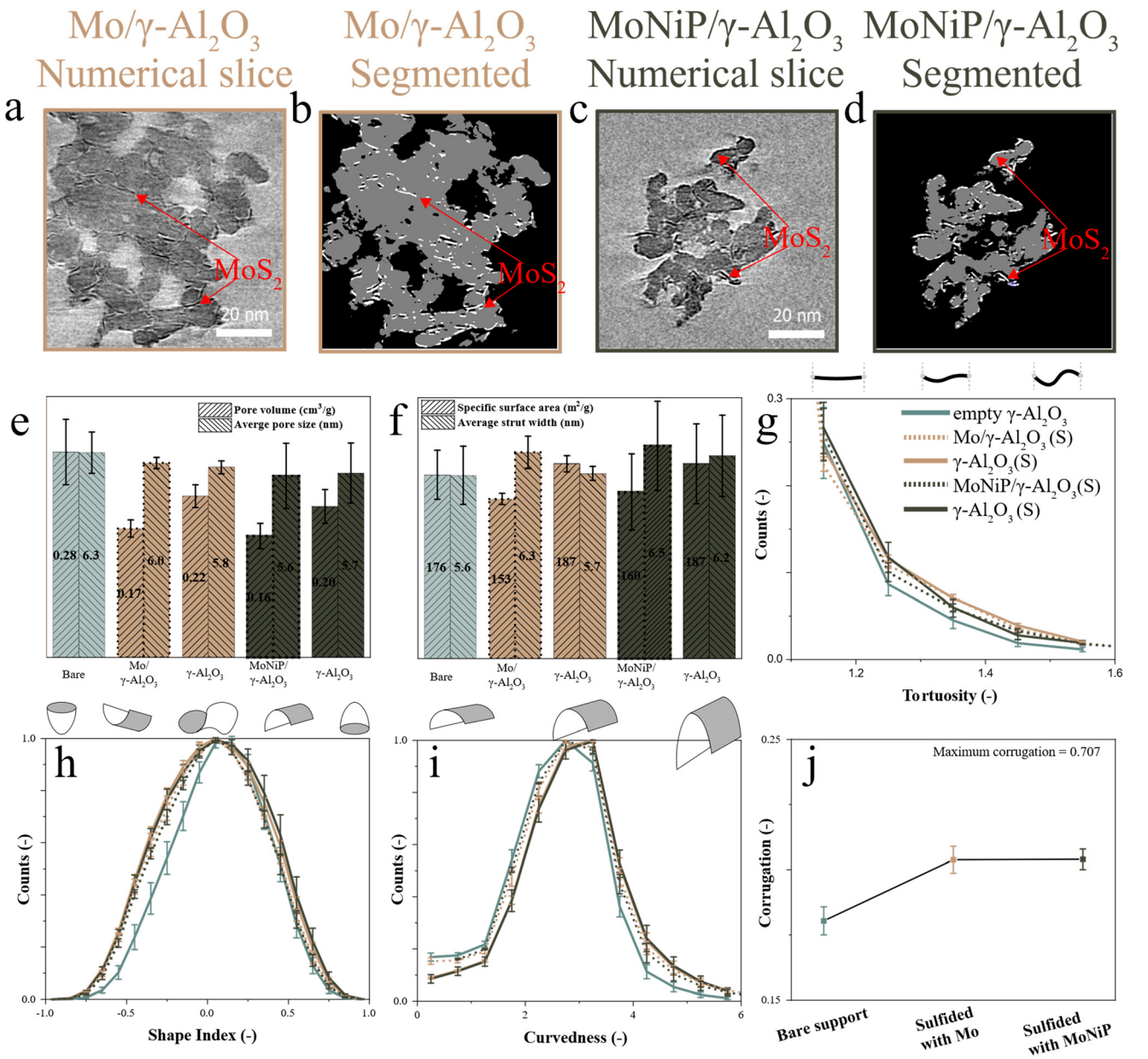

Fig. 3 Quantitative ET showing numerical cross sections (thickness = 0.19 nm) and corresponding segmented cross sections of sulfided γ-Al_2O_3 segmented from the Mo/γ-Al_2O_3 (a and b) and MoNiP/γ-Al_2O_3 (c and d). The γ-Al_2O_3 is compared to the sulfided full solids Mo/γ-Al_2O_3 and MoNiP/γ-Al_2O_3. The formed MoS_2 particles are indicated by red arrows. Quantitative analysis of the surface and pore network showing: (e) PV and average pore size; (f) SSA and average strut width; (g) tortuosity; (h) shape index, (i) curvedness; and (j) surface corrugation.

Open Access Article. Published on 05 2569. Downloaded on 14/5/2569 21:12:59.
This article is licensed under a Creative Commons Attribution 3.0 Unported Licence.

surface and mesopore structure compared to the bare γ-Al_2O_3 support. However, it remains unclear whether these changes are solely due to the solids deposition and transformation, or whether the γ-Al_2O_3 support itself undergoes structural modification. To investigate this, MoS_2 particles were segmented from the γ-Al_2O_3 matrix, allowing for a separate analysis of the support and the active phase. This segmentation, illustrated in Fig. 3(a–d), reveals distinct structural features.

The reliability of this analysis hinges on three key factors: the degree of sulfidation, the imaging accuracy, and the segmentation accuracy. Bulk surface analysis by XPS indicates sulfidation degrees of 73% for Mo/γ-Al_2O_3 and 74% for MoNiP/γ-Al_2O_3, while STEM-EDX indicates values of 79% and 89%, respectively. The large discrepancy observed for MoNiP/γ-Al_2O_3 likely stems from the presence of sulfided Ni species, which can be detected separately by XPS but are indistinguishable from sulfided Mo by STEM-EDX. Incomplete sulfidation results in residual oxidic Mo dispersed over the γ-Al_2O_3 surface, complicating the full isolation of the γ-Al_2O_3 support structure. Additionally, due to the planar, layered structure of MoS_2 and the limitations imposed by the missing wedge in ET, only MoS_2 slabs oriented parallel or slightly tilted (± several degrees) relative to the electron beam at each tilt angle are reliably reconstructed.[87,88] Finally, visual inspection confirms that the segmentation process successfully isolates a representative portion of the MoS_2 slabs, as shown in Fig. 3(b and d). Nonetheless, more sophisticated machine learning segmentation techniques could improve the accuracy of the segmentation, although these methods fall outside the scope of this study. Considering these aspects, we conclude that semi-quantitative analysis is feasible for both the isolated γ-Al_2O_3 support (discussed in the next section) and the MoS_2 slabs (discussed thereafter), while acknowledging the limitations introduced by incomplete sulfidation and the missing wedge.

Surface and mesopore structure of isolated γ-Al_2O_3 after sulfidation

MoS_2 slabs were isolated from the γ-Al_2O_3 matrix in sulfided Mo and MoNiP samples, allowing for a direct comparison between the isolated γ-Al_2O_3 and the fully segmented solids, including bare γ-Al_2O_3, sulfided Mo/γ-Al_2O_3, and sulfided MoNiP/γ-Al_2O_3. The removal of MoS_2 from the γ-Al_2O_3 surface leads to an increase in PV and SSA, a decrease in the strut width; however, no significant change in pore size (Fig. 3(e and f)). These observations suggest that enough MoS_2 was isolated to enable assessment of structural changes in γ-Al_2O_3, induced by sulfidation of Mo or MoNiP.

Irrespective of whether Mo or MoNiP was present during sulfidation, the isolated γ-Al_2O_3 structures exhibited similar PV, SSA, PSD, and strut width. Additionally, compared to the bare γ-Al_2O_3, both systems showed an increase in tortuosity and surface corrugation, with the latter evidenced by a broadening of the shape index curve and increased curvedness (Fig. 3(g–i)). At the bulk scale, changes in the Al environment in the presence of Mo or MoNiP are observed using XPS. In Fig. S3.4(a), XPS spectra of the Al 2p peak exhibit peak broadening after calcination and sulfidation, suggesting changes in the electronic properties, surroundings, and/or metal–support interactions.

The positioning of MoS_2 on the γ-Al_2O_3 surface can be inferred from the effect of slab removal on shape index and curvedness. Upon removal of MoS_2, a broadening of the shape index and curvedness, reflecting increased surface corrugation, is observed relative to the intact Mo/γ-Al_2O_3 and MoNiP/γ-Al_2O_3 samples. This suggests that MoS_2 slabs reside on sharply curved, dome- and cup-like surfaces of the underlying γ-Al_2O_3 surface, which is more corrugated than the bare γ-Al_2O_3 (Fig. 3(j)). Overall, despite differences in precursor chemistry, γ-Al_2O_3 undergoes similar structural changes upon sulfidation in the presence of either Mo or MoNiP, and the resulting MoS_2 particles appear to form in comparable surface locations.

Structural descriptors of isolated MoS_2 slabs

Direct quantification of MoS_2 slabs revealed structural descriptors relevant to the understanding of catalyst functioning. To enable visual inspection of the MoS_2 slabs, a schematic of the shape, as well as the interface with the support and perimeter, as shown in Fig. 4(a), is used to annotate the slabs in Fig. 4. Additionally, key descriptors obtained through XPS, STEM-EDX, and cryo-ET are summarized in Table 2.

The weight loading of Mo and S can be estimated based on the segmented MoS_2. However, the following corrections need to be applied to get a realistic estimate. First, about 30% of the MoS_2 slabs are not (properly) visualized due to the missing wedge (SI, section S6). Second, the distribution of MoS_2 slab thickness needs to be corrected towards the theoretical thickness (0.65 nm). Third, the incomplete sulfidation needs to be accounted for when calculating the total Mo wt%. To this end, the sulfidation degree found through XPS was used. The cryo-ET-derived Mo weight loading present in MoS_2 is 8.7 ± 1.0 wt% and 8.6 ± 2.4 wt% for Mo/γ-Al_2O_3 and MoNiP/γ-Al_2O_3, respectively. The total Mo weight loading (in MoS_2 and MoO_x) is 11.9 ± 1.4 wt% and 11.6 ± 3.3 wt% for Mo/γ-Al_2O_3 and MoNiP/γ-Al_2O_3, respectively, which aligns quite well with XPS and STEM-EDX measurements.

The interface between the MoS_2 slabs and the γ-Al_2O_3 provides insight into slab orientation. Visual inspection, supported by quantitative analysis, reveals a mixture of basal- and edge-plane slab connections to the γ-Al_2O_3. The normalized MoS_2-γ-Al_2O_3 interface areas are 170 m^2 g^{-1} MoS_2 for Mo/γ-Al_2O_3 and 178 m^2 g^{-1} MoS_2 for MoNiP/γ-Al_2O_3, compared to the theoretical maximum of 325 m^2 g^{-1} MoS_2 (SI, section S6). This effect is likely due to the thinner and more uniformly distributed oxidic Mo phase in

 This journal is © The Royal Society of Chemistry 2026

Open Access Article. Published on 05 2569. Downloaded on 14/5/2569 21:12:59.
This article is licensed under a Creative Commons Attribution 3.0 Unported Licence.

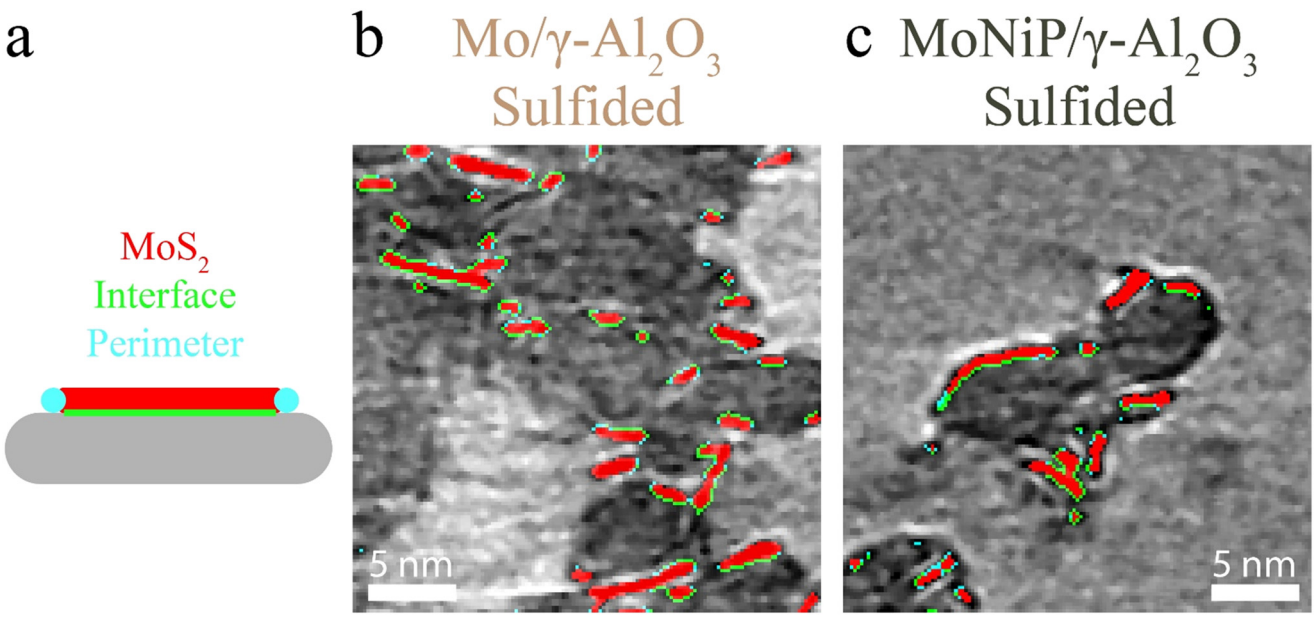

Fig. 4 (a) Schematic of the MoS_2 slab structure on a γ-Al_2O_3 surface. (b) and (c) show a zoom of a numerical slice (thickness = 0.19 nm) through cryo-ET reconstructions of sulfided Mo/γ-Al_2O_3 and MoNiP/γ-Al_2O_3, respectively. The MoS_2 (red), interface (green), and perimeter (cyan) are annotated.

Table 2 XPS, STEM-EDX, and cryo-ET quantification results of MoS_2 slabs

		MoS_2	MoS_2NiP
Mo sulfidation degree (%)	XPS	73 ± 2	74 ± 5
	STEM-EDX	79 ± 6	89 ± 8
S loading (wt%)	XPS	6.5 ± 0.4	6.8 ± 0.3
	STEM-EDX	6.7 ± 0.4	6.6 ± 0.4
	Cryo-ET (in MoS_2)[a]	5.8 ± 0.7	5.7 ± 1.6
Mo loading (wt%)	XPS	9.7 ± 0.4	9.5 ± 0.2
	STEM-EDX	12.0 ± 0.9	10.9 ± 0.5
	Cryo-ET (in MoS_2)[a]	8.7 ± 1.0	8.6 ± 2.4
	Cryo-ET (MoS_2 + MoO_x)[b]	11.9 ± 1.4	11.6 ± 3.3
Structural descriptors found by cryo-ET	Average MoS_2 thickness (nm)	0.51 ± 0.13	0.54 ± 0.05
	MoS_2-γ-Al_2O_3 (m^2 g^{-1} cat)	15.2 ± 3.6	16.1 ± 0.9
	MoS_2-γ-Al_2O_3 (m^2 g^{-1} MoS_2)	170	178
	Total slab perimeter (m^2 g^{-1} cat)	8.1 ± 0.8	6.6 ± 2.0
	Average NN distance (nm)	2.50 ± 0.05	2.70 ± 0.20

[a] Corrected to theoretical thickness and for missing wedge. [b] Corrected to theoretical thickness, for missing wedge, and incomplete sulfidation.

the NiP-promoted catalyst, which, after sulfidation, results in a larger total MoS_2 surface area in contact with the support. A lower interface area suggests a greater proportion of edge-plane connections. Additionally, the total slab perimeter reflects the interface accessible to reactants. The presence of Ni and P results in a smaller average perimeter, although the standard deviation overlaps with the Mo-only system. Finally, the average nearest-neighbor (NN) distance between slabs is comparable for Mo/γ-Al_2O_3 and MoNiP/γ-Al_2O_3.

Establishing correlations between structural descriptors obtained after catalyst preparation and activation, and catalytic performance is crucial in catalysis research. Although no catalytic tests were performed in this study, it is well established that MoNiP/γ-Al_2O_3 exhibits enhanced HDS activity compared to Mo/γ-Al_2O_3 due to the presence of Ni.[33,35,36,89,90] Only small structural differences, accompanied by significant variability, are observed between the slabs in the Mo/γ-Al_2O_3 and MoNiP/γ-Al_2O_3 catalyst. This may suggest that cryo-ET lacks the resolution to capture the promotional effects, which are known to arise from the formation of Ni–Mo–S active sites, where Ni is preferentially located at the sulfur-terminated MoS_2 edges.[90] Moreover, the S-edge/M-edge ratio plays a critical role in catalytic performance and can be tuned through synthesis conditions and additives.[16] Baubet *et al.* demonstrated through high-resolution HAADF-STEM that the 2D shape index of MoS_2 slabs directly correlates with the exposure of M- and S-edges, and thus catalytic activity,[88]

Open Access Article. Published on 05 2569. Downloaded on 14/5/2569 21:12:59.
This article is licensed under a Creative Commons Attribution 3.0 Unported Licence.

highlighting opportunities for the 3D assessment performed in this study. However, achieving such correlations requires higher imaging resolution and more sophisticated segmentation, followed by quantitative 3D slab analysis (*e.g.*, shape index of individual slabs). Exploring these 3D quantitative structure–function relationships at the nanoscale remains largely unexplored for catalysts in general, providing a promising direction for future research.

Conclusions

This study demonstrates the capability of cryo-ET to resolve the 3D surface and mesopore structure of bare γ-Al_2O_3 supports and γ-Al_2O_3-supported hydrotreating catalysts after calcination and subsequent sulfidation. While bare γ-Al_2O_3 largely retains its structural integrity during calcination and sulfidation, cryo-ET reveals subtle variations in surface and pore descriptors that remain inaccessible to bulk characterization techniques. Deposition of oxidic Mo or MoNiP induces modest restructuring of the intrinsic γ-Al_2O_3 structure. The Mo-only catalyst shows more pronounced surface corrugation and pore tortuosity than the MoNiP catalyst, consistent with thicker Mo deposition in the absence of Ni and P, in line with trends observed in bulk characterization and literature. Following sulfidation, both Mo/γ-Al_2O_3 and MoNiP/γ-Al_2O_3 display overall comparable structural characteristics. Visual assessment of the γ-Al_2O_3 and the segmentation of MoS_2 slabs from its surface implies local restructuring of the underlying support. Moreover, slab segmentation indicates that they are preferentially located on sharply curved dome- and cup-like regions of the γ-Al_2O_3 surface. Despite the established influence of P and Ni on MoS_2 morphology and HDS performance, no significant differences in the 3D structural descriptors of the sulfided catalyst were detected. These findings emphasize the need for higher-resolution 3D imaging, more advanced segmentation approaches, and deeper 3D structural analysis to enable robust structure–function correlations capable of establishing a fundamental framework for identifying optimum catalyst configurations beyond the specific catalysts investigated in this study.

Author contributions

J. M. J. J. Heinrichs: conceptualization, data curation, formal analysis, investigation, methodology, project administration, resources, software, validation, visualization, writing – original draft. Th. Weber: conceptualization, funding acquisition, validation, supervision, writing – reviewing & editing. H. Friedrich: conceptualization, validation, supervision, writing – reviewing & editing. J. Zečević: conceptualization, validation, writing – reviewing & editing. A. Evtushkova: formal analysis, investigation, writing – reviewing & editing. E. J. M. Hensen: conceptualization, funding acquisition, validation, supervision, writing – reviewing & editing.

Conflicts of interest

There are no conflicts to declare.

Data availability

The data supporting this article have been included as part of the supplementary information (SI). Supplementary information (SI): S1. Calculation of corrugation value; S2. Untreated, calcined, and sulfided γ-Al_2O_3 – cross sections & segmentation of Fig. 1(a–c), and pore size distribution; S3. Bulk characterization of empty γ-Al_2O_3, Mo/γ-Al_2O_3, and MoNiP/γ-Al_2O_3; S4. Cryo-ET descriptor ranking of empty γ-Al_2O_3, Mo/γ-Al_2O_3, and MoNiP/γ-Al_2O_3; S5. Calcined & sulfided Mo(NiP)/γ-Al_2O_3 – zoom, cross sections & segmentation of Fig. 2(a–d) and S6. Theoretical surface area of MoS_2 and missing wedge correction; S7. References. See DOI: https://doi.org/10.1039/d5cy01396h.

Acknowledgements

This work was part of the Advanced Research Center for Chemical Building Blocks, ARC CBBC, which is co-founded and co-financed by the Dutch Research Council (NOW) and the Netherlands Ministry of Economic Affairs and Climate Policy.

References

1 P. Munnik, P. E. De Jongh and K. P. De Jong, *Chem. Rev.*, 2015, **115**, 6687–6718.
2 H. Arai and M. Machida, *Appl. Catal., A*, 1996, **138**, 161–176.
3 D. L. Trimm, *Catalyst Deactivation*, 1991, **68**, 29–51.
4 P. Yuan, L. Tan, D. Pan, Y. Guo, L. Zhou, J. Yang, J. Zou and C. Yu, *New J. Chem.*, 2011, **35**, 2456–2461.
5 E. Prates Da Costa, X. Huang, C. Kübel, X. Cheng, K. Schladitz, A. Hofmann, U. Göbel and B. M. Smarsly, *Langmuir*, 2023, **39**, 177–191.
6 E. Prates da Costa, X. Huang, C. Kübel, X. Cheng, K. Schladitz, A. Hofmann, U. Göbel and B. M. Smarsly, *Langmuir*, 2023, **39**, 17664–17679.
7 H. Topsøe, B. S. Clausen, R. Candia, C. Wivel and S. Mørup, *J. Catal.*, 1981, **68**, 433–452.
8 H. Topsøe, B. S. Clausen, N.-Y. Topsøe and P. Zeuthen, *Catalysts in Petroleum Refining*, 1989, **53**, 77–102.
9 K. Gishti, A. Iannibello, S. Marengo, G. MorelliLI and P. Tittarelli, *Appl. Catal.*, 1984, **12**, 381–393.
10 A. Salerno and P. A. Netti, in *Biomedical Foams for Tissue Engineering Applications*, Woodhead Publishing Limited, 2014, pp. 3–39.
11 J. A. R. Van Veen, P. A. J. M. Hendriks, R. R. Andréa, E. J. G. M. Romers and A. E. Wilson, *J. Phys. Chem.*, 1990, **94**, 5275–5282.
12 J. A. R. Van Veen, P. A. J. M. Hendriks, R. R. Andréa, E. J. G. M. Romers and A. E. Wilson, *J. Phys. Chem.*, 1990, **94**, 5282–5285.
13 Usman, T. Yamamoto, T. Kubota and Y. Okamoto, *Appl. Catal., A*, 2007, **328**, 219–225.

 This journal is © The Royal Society of Chemistry 2026

Open Access Article. Published on 05 2569. Downloaded on 14/5/2569 21:12:59.
This article is licensed under a Creative Commons Attribution 3.0 Unported Licence.

14 E. J. M. Hensen, V. H. J. De Beer, J. A. R. Van Veen and R. A. Van Santen, *Catal. Lett.*, 2002, **84**, 59–67.
15 J. Liu, W. Y. Li, J. Feng and X. Gao, *J. Fuel Chem. Technol.*, 2021, **49**, 1513–1521.
16 L. Zavala-Sanchez, X. Portier, F. Maugé and L. Oliviero, *Nanotechnology*, 2020, **31**, 035706.
17 S. Eijsbouts, L. C. A. van den Oetelaar, M. Rayner, H. Govaers and T. Boonen, *J. Catal.*, 2021, **403**, 56–73.
18 K. P. De Jong, L. C. A. Van Den Oetelaar, E. T. C. Vogt, S. Eijsbouts, A. J. Koster, H. Friedrich and P. E. De Jongh, *J. Phys. Chem. B*, 2006, **110**, 10209–10212.
19 S. Eijsbouts, X. Li, J. Juan-Alcaniz, L. C. A. Van Den Oetelaar, J. A. Bergwerff, J. Loos, A. Carlsson and E. T. C. Vogt, *ACS Catal.*, 2017, **7**, 4817–4821.
20 M. Li, J. Ihli, M. A. Verheijen, M. Holler, M. Guizar-Sicairos, J. A. Van Bokhoven, E. J. M. Hensen and Th. Weber, *J. Phys. Chem. C*, 2022, **126**, 18536–18549.
21 J. Ihli, L. Bloch, F. Krumeich, K. Wakonig, M. Holler, M. Guizar-Sicairos, T. Weber, J. C. da Silva and J. A. van Bokhoven, *Angew. Chem., Int. Ed.*, 2020, **59**, 17266–17271.
22 B. Baubet, E. Devers, A. Hugon, E. Leclerc and P. Afanasiev, *Appl. Catal., A*, 2014, **487**, 72–81.
23 J. Chen, L. Oliviero, X. Portier and F. Maugé, *RSC Adv.*, 2015, **5**, 81038–81044.
24 D. Zhang, W. Q. Liu, Y. A. Liu, U. J. Etim, X. M. Liu and Z. F. Yan, *Chem. Eng. J.*, 2017, **330**, 706–717.
25 D. Zhang, X. M. Liu, Y. X. Liu and Z. F. Yan, *Microporous Mesoporous Mater.*, 2021, **310**, 110637.
26 X. Liu, X. Li and Z. Yan, *Appl. Catal., B*, 2012, **121–122**, 50–56.
27 S. Badoga, R. V. Sharma, A. K. Dalai and J. Adjaye, *Appl. Catal., A*, 2015, **489**, 86–97.
28 E. D. Garcia, *PhD thesis*, Normandie Université, 2018.
29 L. Catita, A. A. Quoineaud, D. Espinat, C. Pichon and O. Delpoux, *Appl. Catal., A*, 2017, **547**, 164–175.
30 B. Barata, C. Legens, E. Devers, O. Delpoux, L. Barthe, O. Roudenko and V. Briois, *ChemCatChem*, 2023, **2023**, e202201440.
31 V. S. Marakatti, D. Mumbaraddi, G. V. Shanbhag, A. B. Halgeri and S. P. Maradur, *RSC Adv.*, 2015, **5**, 93452–93462.
32 M. Adachi, C. Contescu and J. A. Schwarz, *J. Catal.*, 1996, **158**, 411–419.
33 G. M. Bremmer, L. van Haandel, E. J. M. Hensen, J. W. M. Frenken and P. J. Kooyman, *Appl. Catal., B*, 2019, **243**, 145–150.
34 L. van Haandel, G. M. Bremmer, E. J. M. Hensen and Th. Weber, *J. Catal.*, 2017, **351**, 95–106.
35 L. S. Byskov, J. K. Nørskov, B. S. Clausen and H. Topsøe, *J. Catal.*, 1999, **187**, 109–122.
36 M. Egorova and R. Prins, *J. Catal.*, 2006, **241**, 162–172.
37 C. Cottrez, S. Humbert, A. S. Gay, E. Devers, F. De Geuser, C. Legens, X. Carrier and A. Chaumonnot, *ChemCatChem*, 2025, e202401670.
38 P. Priecel, D. Kubička, A. Vázquez-Zavala, J. A. de los Reyes, M. Pouzar and L. Čapek, *Front. Chem.*, 2020, **8**, 216.
39 H. Wang, J. Wu, Z. Xiao, Z. Ma, P. Li, X. Zhang, H. Li and X. Fang, *Catal. Sci. Technol.*, 2021, **11**, 1125–1140.
40 Th. Weber, J. C. Muijsers, J. H. M. C. Van Wolput, C. P. J. Verhagen and J. W. Niemantsverdriet, *J. Phys. Chem.*, 1996, **100**, 14144–14150.
41 P. Kumar, S. K. Maity and D. Shee, *ACS Omega*, 2019, **4**, 2833–2843.
42 X. Ma, K. Cui, W. Hao, R. Ma, Y. Tian and Y. Li, *Bioresour. Technol.*, 2015, **192**, 17–22.
43 S. R. Yenumala, P. Kumar, S. K. Maity and D. Shee, *Bioresour. Technol. Rep.*, 2019, **7**, 100288.
44 A. Afshar Taromi and S. Kaliaguine, *Fuel Process. Technol.*, 2018, **171**, 20–30.
45 J. Hu, L. Yu, J. Deng, Y. Wang, K. Cheng, C. Ma, Q. Zhang, W. Wen, S. Yu, Y. Pan, J. Yang, H. Ma, F. Qi, Y. Wang, Y. Zheng, M. Chen, R. Huang, S. Zhang, Z. Zhao, J. Mao, X. Meng, Q. Ji, G. Hou, X. Han, X. Bao, Y. Wang and D. Deng, *Nat. Catal.*, 2021, **4**, 242–250.
46 Y. Y. Chen, M. Dong, J. Wang and H. Jiao, *J. Phys. Chem. C*, 2012, **116**, 25368–25375.
47 H. Y. Su, W. Liao and K. Sun, *Catal. Sci. Technol.*, 2024, **14**, 2608–2618.
48 M. Trueba and S. P. Trasatti, *Eur. J. Inorg. Chem.*, 2005, **2005**, 3393–3403.
49 C. Schlumberger and M. Thommes, *Adv. Mater. Interfaces*, 2021, **8**, 2002181.
50 K. A. Cychosz and M. Thommes, *Engineering*, 2018, **4**, 559–566.
51 R. Cimino, K. A. Cychosz, M. Thommes and A. V. Neimark, *Colloids Surf., A*, 2013, **437**, 76–89.
52 Z. Wang, J. Huang, G. Jiang, T. Ji, H. Lin, L. Mu and J. Zhu, *Chem. Mater.*, 2025, **37**, 1337–1348.
53 S. Kolitcheff, E. Jolimaitre, A. Hugon, J. Verstraete, P. L. Carrette and M. Tayakout-Fayolle, *Microporous Mesoporous Mater.*, 2017, **248**, 91–98.
54 T. M. Eggenhuisen, J. Zečević, H. Talsma, K. P. De Jong and P. E. De Jongh, *J. Phys. Chem. C*, 2012, **116**, 7480–7490.
55 J. A. Bergwerff, L. G. A. Van De Water, T. Visser, P. De Peinder, B. R. G. Leliveld, K. P. De Jong and B. M. Weckhuysen, *Chem. – Eur. J.*, 2005, **11**, 4591–4601.
56 E. K. Gibson, M. W. Zandbergen, S. D. M. Jacques, C. Biao, R. J. Cernik, M. G. O'Brien, M. Di Michiel, B. M. Weckhuysen and A. M. Beale, *ACS Catal.*, 2013, **3**, 339–347.
57 T. M. Eggenhuisen, M. J. Van Steenbergen, H. Talsma, P. E. De Jongh and K. P. De Jong, *J. Phys. Chem. C*, 2009, **113**, 16785–16791.
58 L. Espinosa-Alonso, A. A. Lysova, P. De Peinder, K. P. De Jong, I. V. Koptyug and B. M. Weckhuysen, *J. Am. Chem. Soc.*, 2009, **131**, 6524–6534.
59 A. A. Lysova, *Appl. Magn. Reson.*, 2014, **45**, 1359–1375.
60 A. A. Lysova, J. A. Bergwerff, L. Espinosa-Alonso, B. M. Weckhuysen and I. V. Koptyug, *Appl. Catal., A*, 2010, **374**, 126–136.
61 A. A. Lysova, I. V. Koptyug, R. Z. Sagdeev, V. N. Parmon, J. A. Bergwerff and B. M. Weckhuysen, *J. Am. Chem. Soc.*, 2005, **127**, 11916–11917.

Open Access Article. Published on 05 2569. Downloaded on 14/5/2569 21:12:59.
This article is licensed under a Creative Commons Attribution 3.0 Unported Licence.

62 I. Arslan, J. C. Walmsley, E. Rytter, E. Bergene and P. A. Midgley, *J. Am. Chem. Soc.*, 2008, **130**, 5716–5719.
63 F. Nan, C. Song, J. Zhang, R. Hui, J. Chen, C. Fairbridge and G. A. Botton, *ChemCatChem*, 2011, **3**, 999–1003.
64 R. Grothausmann, G. Zehl, I. Manke, S. Fiechter, P. Bogdanoff, I. Dorbandt, A. Kupsch, A. Lange, M. P. Hentschel, G. Schumacher and J. Banhart, *J. Am. Chem. Soc.*, 2011, **133**, 18161–18171.
65 M. Ko, E. Padgett, V. Yarlagadda, A. Kongkanand and D. A. Muller, *J. Electrochem. Soc.*, 2021, **168**, 024512.
66 L. Q. Wagner, E. Prates da Costa, C. Glatthaar, F. Breckwoldt, M. Zecca, P. Centomo, X. Huang, C. Kübel, H. Schlaad, M. Kriechbaum, H. Amenitsch, M. Thommes and B. M. Smarsly, *Chem. Mater.*, 2023, **35**, 9879–9899.
67 J. Zečević, K. P. De Jong and P. E. De Jongh, *Curr. Opin. Solid State Mater. Sci.*, 2013, **17**, 115–125.
68 Y. Yao, K. J. Czymmek, R. Pazhianur and A. M. Lenhoff, *Langmuir*, 2006, **22**, 11148–11157.
69 E. P. W. Ward, T. J. V. Yates, J. J. Fernández, D. E. W. Vaughan and P. A. Midgley, *J. Phys. Chem. C*, 2007, **111**, 11501–11505.
70 J. Marqueses-Rodríguez, R. Manzorro, J. Grzonka, A. J. Jiménez-Benítez, L. C. Gontard, A. B. Hungría, J. J. Calvino and M. López-Haro, *Chem. Mater.*, 2023, **35**, 7564–7576.
71 G. Prieto, J. Zečević, H. Friedrich, K. P. De Jong and P. E. De Jongh, *Nat. Mater.*, 2013, **12**, 34–39.
72 A. B. Hungría, J. J. Calvino and J. C. Hernández-Garrido, *Top. Catal.*, 2019, **62**, 808–821.
73 S. Eijsbouts, L. Van Gruijthuijsen, J. Volmer, V. H. J. De Beer and R. Prins, *J. Catal.*, 1991, **131**, 412–432.
74 J. C. Muijsers, Th. Weber, R. M. Vanhardeveld, H. W. Zandbergen and J. W. Niemantsverdriet, *J. Catal.*, 1995, **157**, 698–705.
75 L. Van Haandel, M. Bremmer, P. J. Kooyman, J. A. R. Van Veen, Th. Weber and E. J. M. Hensen, *ACS Catal.*, 2015, **5**, 7276–7287.
76 J. Ayache, L. Beaunier, J. Boumendil, G. Ehret and D. Laub, *Sample Preparation Handbook for Transmission Electron Microscopy - Methodology*, Springer, 2010.
77 J. R. Kremer, D. N. Mastronarde and J. R. McIntosh, *J. Struct. Biol.*, 1996, **116**, 71–76.
78 D. N. Mastronarde, *J. Struct. Biol.*, 1997, **120**, 343–352.
79 D. N. Mastronarde and S. R. Held, *J. Struct. Biol.*, 2017, **197**, 102–113.
80 S. Berg, D. Kutra, T. Kroeger, C. N. Straehle, B. X. Kausler, C. Haubold, M. Schiegg, J. Ales, T. Beier, M. Rudy, K. Eren, J. I. Cervantes, B. Xu, F. Beuttenmueller, A. Wolny, C. Zhang, U. Koethe, F. A. Hamprecht and A. Kreshuk, *Nat. Methods*, 2019, **16**, 1226–1232.
81 C. Sommer, C. Straehle, U. Köthe and F. A. Hamprecht, *IEEE Int. Symp. Biomed. Imaging*, 2011, DOI: 10.1109/ISBI.2011.5872394.
82 J. J. Koenderink and A. J. van Doorn, *Image Vis. Comput.*, 1992, **10**, 557–564.
83 J. M. J. J. Heinrichs, R. R. M. Joosten, J. Zecevic, Th. Weber, E. J. M. Hensen and H. Friedrich, *Chem. Methods*, 2025, **00**, e202500115.
84 L. van Haandel, *PhD Thesis*, Eindhoven University of Technology, 2016.
85 C. Ophus, *Microsc. Microanal.*, 2019, **25**, 563–582.
86 E. Yücelen, I. Lazić and E. G. T. Bosch, *Sci. Rep.*, 2018, **8**, 1–10.
87 G. M. Bremmer, L. Van Haandel, E. J. M. Hensen, J. W. M. Frenken and P. J. Kooyman, *J. Phys. Chem. C*, 2016, **120**, 19204–19211.
88 B. Baubet, M. Girleanu, A. S. Gay, A. L. Taleb, M. Moreaud, F. Wahl, V. Delattre, E. Devers, A. Hugon, O. Ersen, P. Afanasiev and P. Raybaud, *ACS Catal.*, 2016, **6**, 1081–1092.
89 F. Pelardy, A. S. dos Santos, A. Daudin, E. Devers, T. Belin and S. Brunet, *Appl. Catal., B*, 2017, **206**, 24–34.
90 S. Rangarajan and M. Mavrikakis, *ACS Catal.*, 2017, **7**, 501–509.

This journal is © The Royal Society of Chemistry 2026